RESEARCH ARTICLE

Enhanced osteogenesis and bactericidal performance of additively manufactured MgO- and Cu-added CpTi for load-bearing implants

Sushant Ciliveri, and Amit Bandyopadhyay*

W. M. Keck Biomedical Materials Research Laboratory, School of Mechanical and Materials Engineering, Washington State University, Pullman, WA 99164, USA

(This article belongs to the *Special Issue: 3D Bioprinting for Materials and Application*)

Abstract

The bio-inertness of titanium, which is the ultimate choice of metallic material for implant applications, causes delayed bone–tissue integration at the implant site and prevents expedited healing for the patient. This can result in a severe issue for patients with immunocompromised bone health as titanium does not offer inherent antimicrobial properties, and thus, infections at the implant site are another concern. Current strategies addressing the issues above include using cemented implants as a coating on Ti6Al4V bulk material for orthopedic applications. Roadblock arises with coating failure due to weak interfacial bond at the Ti–cement interface, which necessitates revision surgeries. In this study, we added osteogenic MgO and antibacterial Cu to commercially pure titanium (CpTi) and processed them using metal additive manufacturing. Mg, an essential trace element in the body, has been proven to enhance osseointegration *in vivo*. Cu has been popular for its bactericidal capabilities. With the addition of 1 wt.% of MgO to the CpTi matrix, we observed a four-fold increase in the mineralized bone formation at the bone–implant interface *in vivo*. The addition of 3 wt.% of Cu did not result in cytotoxicity, and adding Cu to CpTi-MgO chemical makeup yielded *in vivo* performance similar to that in CpTi-MgO. In *in vitro* bacterial studies with gram-positive *Staphylococcus aureus*, CpTi-MgO-Cu displayed an antibacterial efficacy of 81% at the end of 72 h of culture. Our findings highlight the synergistic benefits of CpTi-MgO-Cu, which exhibit superior early-stage osseointegration and antimicrobial capabilities.

Keywords: Commercially pure titanium; Osseointegration; Additive manufacturing; Antibacterial performance; Porous metal

*Corresponding authors:
Amit Bandyopadhyay
(amitband@wsu.edu)

1. Introduction

The selection of metallic materials for biomedical applications relies on several considerations, including corrosion resistance, fatigue strength, and biocompatibility[1,2]. Over the years, titanium (Ti) has emerged as the optimal material for load-bearing implants[3-5]. While Ti6Al4V demonstrates excellent fatigue resistance and is commonly used for bulk metallic implants at load-bearing sites[6], commercially pure titanium (CpTi) with higher biocompatibility but lower strength than Ti6Al4V is often employed either at low-load-bearing sites or as a metallic coating on these bulk implants[7]. Since

the *in vivo* performance of an implant is greatly influenced by the chemistry of the implant surface upon contact with the physiological environment, researchers have explored the use of calcium phosphate (CaP) coatings added with dopants, such as MgO, SiO_2, and ZnO, on bulk Ti to enhance osseointegration[8-10]. However, the weak metal-ceramic interface in these coatings has led to challenges, including some coating failures due to delamination.

The long-term stability of the implant is severely affected by polymicrobial infections at the implant site, eventually leading to implant loosening and prosthetic joint infection (PJI)[11]. Addressing such polymicrobial infections involves long-term antibiotic administration, revision surgeries involving debridement of infected tissues with implant retention, or implant replacement, the latter being the most effective in eradicating the infection[12-14]. However, revision surgeries in patients with compromised bone health pose significant risks to their overall well-being and increase the probability of early mortality. A report on PJI indicated that 25% of patients treated for PJI died within 5 years[15]. Moreover, a recent survey by the World Health Organization highlights 700,000 annual deaths due to microbial infections, with projections of 10 million deaths by 2050[16]. The seriousness of the situation prompted a call to action at the United Nations General Assembly in 2017, aiming to reduce the mortality caused by antimicrobial resistance down by 200,000 deaths[18]. Without adequate intervention, the number of deaths from polymicrobial infections may rise exponentially in the coming decades.

Despite titanium's established position as the ultimate metallic material for implant applications worldwide, its bio-inertness remains a significant drawback[17,18]. The early stage of osseointegration, which is crucial for a patient's healing period post-surgery and the long-term stability *in vivo*, can be severely affected by a prolonged healing process at the implant site, particularly in individuals with compromised bone health. Given that the implant's surface is constantly in contact with the physiological environment, its role in biological performance, including osseointegration and integration with surrounding bone tissue, is vital. Numerous strategies have been employed to enhance bone–tissue integration on titanium surfaces, such as introducing surface porosities and calcium phosphate coatings with dopant additions. One prominent dopant addition is magnesium oxide (MgO), which enhances osteogenesis in bone-remodeling processes. Magnesium (Mg) is the fourth main cation found in the human body; an adult body contains approximately 25 g of Mg, with 50–60% present in the bony intracellular matrix[19]. Mg, a biodegradable material *in vivo* with poor corrosion resistance, is usually incorporated in a biomaterial matrix

such as hydroxyapatite[20]. Mg^{2+} ions play a crucial role in bone metabolism, aiding osteogenesis by regulating local pH, which enhances osteoblast recruitment, proliferation, and differentiation[21,22]. Mg^{2+} ions also aid in regulating gene expressions in stem cell differentiation of osteoblastic cells to stimulate formation of bone matrix proteins and enhance bone formation[23,24]. Numerous studies have demonstrated the efficacy of Mg ions in bioactive ceramic matrices, significantly enhancing cell proliferation *in vitro*[25,26] and osteogenesis and bone mineralization *in vivo*[8,27].

A major concern associated with cemented implants is aseptic loosening due to delamination of the ceramic coating on the titanium implant under loading conditions, leading to implant failure[28-31]. A recent survey study on the aseptic loosening of cemented implants post-total knee arthroplasty surgeries from 2009 to 2017 reported an alarming 6% failure rate due to cement debonding in the tibial implant[32]. Such a high failure rate necessitates a search for suitable cemented implant substitutes. Instead of using Mg-doped hydroxyapatite or calcium phosphate cemented onto titanium implants, we propose incorporating MgO into the Ti matrix. Limited studies have been conducted on incorporating MgO into the metal matrix to enhance osteogenesis[25]. The challenges posed by the difference in melting points between Ti (1668°C) and MgO (2852°C) have been overcome by utilizing additive manufacturing (AM) for fabricating this composition. AM allows the manufacturing of metal-ceramic composites with greater flexibility and enables the incorporation of designed porosities that aid in enhanced osseointegration *in vivo*, a feat not achievable by other manufacturing methods[33]. However, to prevent brittleness of the metal-ceramic composites and ensure successful AM fabrication, we have restricted the addition of MgO dopant to 1 wt.% in Ti[34]. Copper (Cu) has also been extensively studied due to its antibacterial properties in Ti-Cu alloys. Nevertheless, concerns regarding toxicity resulting from higher amounts of Cu in the human body limit its use in significant quantities. This study added small amounts of Cu (3 wt.%) to the Ti-MgO composition.

Given these issues, we added MgO and Cu to CpTi matrix to enhance its osteogenic potential and imbue inherent bactericidal capabilities. There lies a research gap in exploring the effect of MgO incorporation into Ti matrix. The novelty of this study lies in investigating the synergistic osteogenic and antibacterial potential of the CpTi-MgO-Cu material design. This Ti-MgO-Cu material chemistry is expected to enhance early-stage osseointegration due to osteogenic MgO and prevent polymicrobial infection incidence at the implant site,

ensuring the implant's long-term stability and preventing the need for revision procedures due to their aseptic loosening. This study aims to fabricate CpTi, CpTi + 1 wt.% MgO (CpTi-MgO), and CpTi + 1 wt.% MgO + 3 wt.% Cu (CpTi-MgO-Cu) compositions using metal AM. These compositions were characterized in terms of their microstructure and microhardness. *In vivo* rat studies were conducted to evaluate the biological performance of these compositions. Structures utilized for the *in vivo* studies were ~40 vol.% porous with an approximate pore size of 600–700 μm since pore sizes in this range are optimum for enhanced tissue integration and osseointegration[35,36]. Additionally, *in vitro* bacterial culture was studied using the commonly occurring *Staphylococcus aureus* strain to evaluate the antibacterial efficacy of CpTi-MgO-Cu. We hypothesize that the CpTi-MgO-Cu composition will demonstrate better osseointegration performance than CpTi *in vivo* with no cytotoxicity due to the presence of Cu, as schematically shown in Figure 1.

2. Materials and methods

2.1. Processing of samples using metal additive manufacturing

CpTi, CpTi-MgO, and CpTi-MgO-Cu compositions were processed using metal additive manufacturing. A metal matrix composition of CpTi-MgO was prepared by premixing CpTi powders (GKN Hoeganaes, Cinnaminson, NJ, USA) with 1 wt.% of MgO (Inframat® Advanced Materials™, Manchester, CT, USA) powders. Similarly, CpTi-MgO-Cu composition was prepared by premixing CpTi powders with 1 and 3 wt.% of MgO and Cu (GKN Hoeganaes, Cinnaminson, NJ, USA) powders, respectively. All metal and ceramic powders used for fabrication were sieved to obtain a powder particle size of <63 μm. All metal

and ceramic powers used were spherical. The fabrication used two AM processes: directed energy deposition (DED) and selective laser melting (SLM). Samples for *in vitro* study were printed on a 5-axis DED-based AM system (FormAlloy, Spring Valley, CA). Although coarser powder particles (45–150 μm) are preferred for DED-based AM systems, we optimized the printing parameters to accommodate finer particle size of <63 μm for the printing operation. The printing operation was conducted in an argon-purged environment with O_2 < 20 ppm in the printing chamber. A cold rolled CpTi substrate was used as a build plate. Discs of 8 mm diameter and 4 mm height were printed on the DED system. The printing parameters used for the compositions are presented in Table 1.

Samples used for *in vivo* study were printed on an SLM-based powder bed fusion system (3D Systems ProX® DMP 200, Rock Hill, SC, USA) with a 300 W fiber laser and a wavelength of λ = 1070 nm. Porous structures of 2.4 mm diameter and 4 mm height with ~40 vol.% porosity were designed in 3DXpert CAD Software (3D Systems, Rock Hill, SC, USA). Premixed powders were poured into the supply chamber and compacted using a compaction plate. A thick CpTi plate of ~2.5 cm thickness was used as the build platform and secured on the melting stage. A roller system carried powders from the supply to the build stage, with 30 μm set as the layer thickness. The laser power and scanning speed for all the compositions are reported in Table 1. 3D Systems provide printing parameters used for CpTi and CpTi-MgO as the standard Ti printing parameters. Laser power was increased by 10%, and scan speed reduced by 10% to increase the print energy input for CpTi-MgO-Cu since Cu displays poor laser absorption and needs more energy for additive manufacturing operation[37,38]. Post-printing porous cylinders were cut from the build plate and
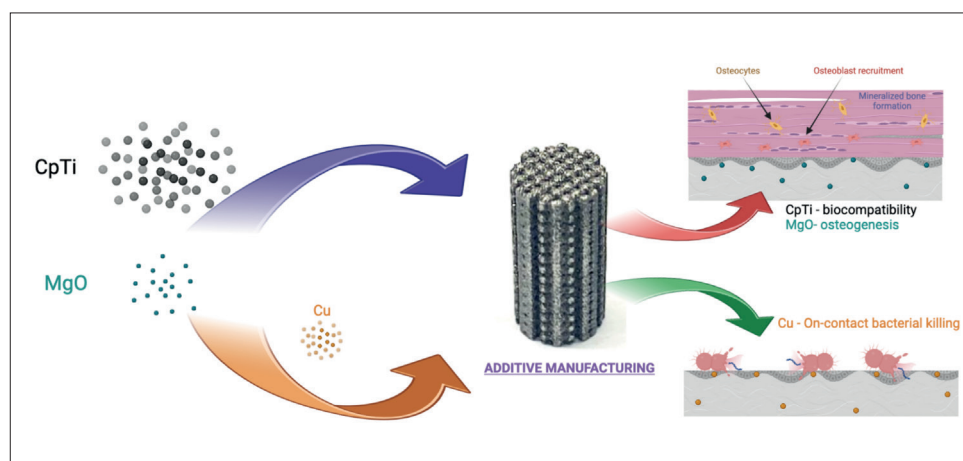

Figure 1. Schematic of MgO-induced osteogenic activity toward early-stage osseointegration and bactericidal effect of Cu in CpTi. The CpTi-MgO-Cu was processed via metal additive manufacturing, enabling the incorporation of designed porosity. This further expedites the bone remodeling and tissue attachment on the implant's surface, contributing to its long-term stability *in vivo*.

Table 1. Print-processing parameters used for DED and PBF operations of additively manufactured CpTi, CpTi-MgO, and CpTi-MgO-Cu compositions

	DED (*in vitro*, microstructure, hardness)							
Composition	Laser power (W)		Scan speed (mm/min)		Shield gas (ℓ/min)	Carrier gas (ℓ/min)	Powder disc speed (rpm)	Slice (mm)
	Contour	Hatch	Contour	Hatch				
CpTi								
CpTi-MgO	350	350	1500	1200	18	14	0.7	0.3
CpTi-MgO-Cu								

	PBF (*in vivo*, ~40% porosity)		
Composition	Laser power (W)	Scan speed (mm/s)	Slice (μm)
CpTi			
CpTi-MgO	180	1600	30
CpTi-MgO-Cu	198	1440	

subjected to repeated sonication in deionized water and ethanol, followed by compressed air treatment to remove any loose powder particles inside the pores. The final step in residual powder removal involved acid etching in 1% hydrogen fluoride in deionized water. The samples were sonicated again in deionized water and ethanol to remove any acid residues.

2.2. Microhardness and microstructure
DED-printed discs were cut off the build plate and subjected to grinding on silicon carbide grinding papers with 80–2000 grit size. This was followed by alumina suspension polishing to reduce the alumina powder particle size from 1 to 0.05 μm. Vickers microhardness test was conducted on a Phase II Plus Micro Vickers Hardness tester (Upper Saddle River, NJ, USA) using a load of 200 g and a dwell time of 15 s. Hardness values on a polished surface perpendicular to the build direction were obtained. An n = 5 measurement were taken for each composition. For acquiring the microstructures, polished surfaces of the discs were etched in Kroll's reagent for 45 s and observed under a scanning electron microscope (SEM; Apreo, Thermo Scientific, MA, USA).

2.3. *In vitro* bacterial study
Bacterial culture was carried out on CpTi and CpTi-MgO-Cu to evaluate the antibacterial resistance using gram-positive *S. aureus* strain for 24, 48, and 72 h. Freeze-dried *S. aureus* (Carolina Biological, NC, USA) was rehydrated using rehydration media. Tryptic soy broth was used as the nutrient medium. The rehydrated bacterium was subjected to nutrient broth dilutions to obtain 0.5 McFarland standard optical density measurement corresponding to 10^8 CFU/ml of bacteria. Polished disc samples were sterilized before culture, placed in 24-well plates, and then studied in triplicate for colony count on agar plate and in duplicate

for SEM characterization. Bacterial colonies at 10^6 CFU of bacterial colonies were seeded on the surface of the discs, with 2 ml of tryptic soy broth added as the nutrient medium in each well. After the respective time points, bacterial cells from triplicate samples for agar plate colony count were scraped using cell scrapers and mixed in 2 ml of 0.1 M PBS, which was then serially diluted to approximately 10 to 100 colonies in 1 μl of the solution. One microliter of this solution was streaked on a tryptic soy agar plate and incubated for 24 h. The duplicate samples used to observe the bacterial cell morphology were subjected to fixative solution overnight. Dehydration was carried out with 2% OsO4 (Osmium tetroxide), followed by ethanol and HMDS dehydration treatments. The samples were gold coated and observed under an SEM (Quanta 200F, Thermo Fisher, Waltham, USA). Images were taken at 300× magnification for each composition, and the number of bacterial cells was counted on at least n = 4 images for each composition. The antibacterial efficacy for agar plate count at 24 h was evaluated as a function of bacterial colonies counted on individual material compositions, as

$$N = C \times d \times 1000/l$$

$$R = (N_{control} - N_{material})/N_{control} \times 100\%$$

where N is the calculated number of bacterial colonies observed, C is the average colony count on a plate, d is the dilution factor, and l is the volume of bacterial suspension on the sample. Antibacterial efficacy from SEM images was evaluated at 24, 48, and 72 h timepoints and calculated for R, with N being the average number of bacterial cells from multiple SEM images.

2.4. *In vivo* study
CpTi, CpTi-MgO, and CpTi-MgO-Cu compositions were subjected to an *in vivo* rat study. CpTi is known to

demonstrate excellent *in vivo* biological performance and is used as a control. Adding MgO to CpTi is expected to yield better early-stage osseointegration performance than CpTi. PBF-fabricated porous implants with ~40 vol.% porosity were used for the study.

2.4.1. Surgery and implantation procedure

Male Sprague-Dawley rats with average weights between 300 and 350 g were used for the *in vivo* study. The animals were acclimatized in temperature- and humidity-controlled rooms in separate cages for at least 2 weeks. Buprenorphine (0.3 mg/kg) was subcutaneously administered to the animals for alleviating pain 30 min before anesthesia. A prescribed dose of IsoFlo® (isoflurane, USP, Abbott Laboratories, North Chicago, IL, USA) coupled with oxygen (Oxygen USP, A-L Compressed Gases Inc., Spokane, WA, USA) was used to anesthetize the animals. Once the animal's movements ceased under anesthesia, the implantation area around the femur and the knee was shaved thoroughly and cleaned thrice with chlorhexidine and isopropyl alcohol scrubs. Lidocaine hydrochloride (0.3 ml; without epinephrine) with a 0.5% concentration was subcutaneously administered as a localized numbing agent near the implantation area on each limb. The animal was then transferred onto a sterile surgery table area. A 2-inch incision was made along the femur on the lateral side above the distal femoral condyle. A unicortical defect of 2.4 mm diameter was made on the lateral epicondyle using gradually increasing drill bits and rinsed with saline to prevent thermal necrosis and remove bone fragments. The implant was inserted, and the fascia and the skin over the incision were sutured with undyed braided coated with MONOCRYL-polyglactin 910 (Ethicon Inc., Somerville, NJ, USA). The incision area was cleaned with saline scrubs and stapled. A similar procedure was carried out on the other limb of the animal. The animal was periodically monitored for its breathing rate during the surgery procedure. Lactated ringers solution (LRS, 3 ml) for rehydration was subcutaneously administered to the animal post-surgery, followed by meloxicam (0.2 mg/kg) administration as an anti-inflammatory analgesic, and monitored until the animal regained consciousness. Post-operative care was carried out for 3 days, with buprenorphine administration every 12 h and meloxicam every 24 h. The animals were euthanized 6 weeks after the surgery by means of carbon dioxide overdose, followed by cervical dislocation as a secondary measure, and the femoral bone with the metal implant was harvested. The Institutional Animal Care and Use Committee (IACUC) of Washington State University (WSU-Pullman, WA)-approved protocol was followed to perform the experimental and surgical procedure.

2.4.2. Histological and histomorphometric analysis

The bone–metal explants were fixed in 10% neutral buffered formalin for at least 72 h for tissue infiltration. Serial dehydration was carried out in ethanol followed by embedment in polymethylmethacrylate (PMMA)[39]. These embedded bone explants were cut on Ekakt™ saw into 200 μm thick sections, mounted on glass slides, and then ground to 20–50 μm thick sections using sand paper with 1200 grit size on Ekakt 400 micro grinder. The sections were then polished on the micro grinder using paper with 4000 grit size. Gomori trichrome, hematoxylin & eosin (H&E), and Sanderson's Rapid Bone Staining (SRBS) were used to stain separate bone sections for each composition. The stained bone sections were imaged on a Keyence digital microscope (Model VHX-7000, Itasca, IL, USA). H&E-stained slides were imaged for any visible markers that indicate an inflammatory response in areas around the implant. Gomori's trichrome-stained slides were observed for the presence of muscle fibers and collagen at the bone–implant contact (BIC), and SRBS-stained slides for the mineralized bone formation, osteoid presence at the BIC, and mineralization fronts.

Histomorphometric analysis was carried out using SRBS-stained slides for each composition. To restrict the region of interest (ROI) to 100–150 μm from the implant surface, images were captured at 1000× magnification around the BIC region. Quantitative evaluation of mineralized bone formation at the BIC was carried out using Trainable Weka Segmentation in ImageJ with Random Forest Algorithm for individual images[40,41]. At least seven regions were analyzed to quantify mineralized bone formation at the BIC, which was expressed in % area fraction.

3. Results

CpTi shows good biocompatibility and no cytotoxicity. Compared to bulk Ti6Al4V implants, CpTi is a more popular coating material choice owing to the lack of strength and fatigue resistance. However, it is bio-inert and possesses no antibacterial capabilities. Besides, the surface properties of the implant influence its biological performance in the physiological environment. This study aims to enhance the early-stage osseointegration of CpTi by adding MgO and to induce inherent antibacterial capabilities by adding Cu. This CpTi-MgO-Cu material chemistry is expected to show superior biological performance *in vivo* compared to CpTi and can be a potential metallic coating material of choice for bulk metallic implants.

3.1. Microstructure and hardness

SEM micrographs of the etched surface for CpTi and CpTi-MgO (Figure 2b) show typical α' martensitic needle-like structures typically observed in additively manufactured CpTi due to the fast-cooling nature of the process[42].
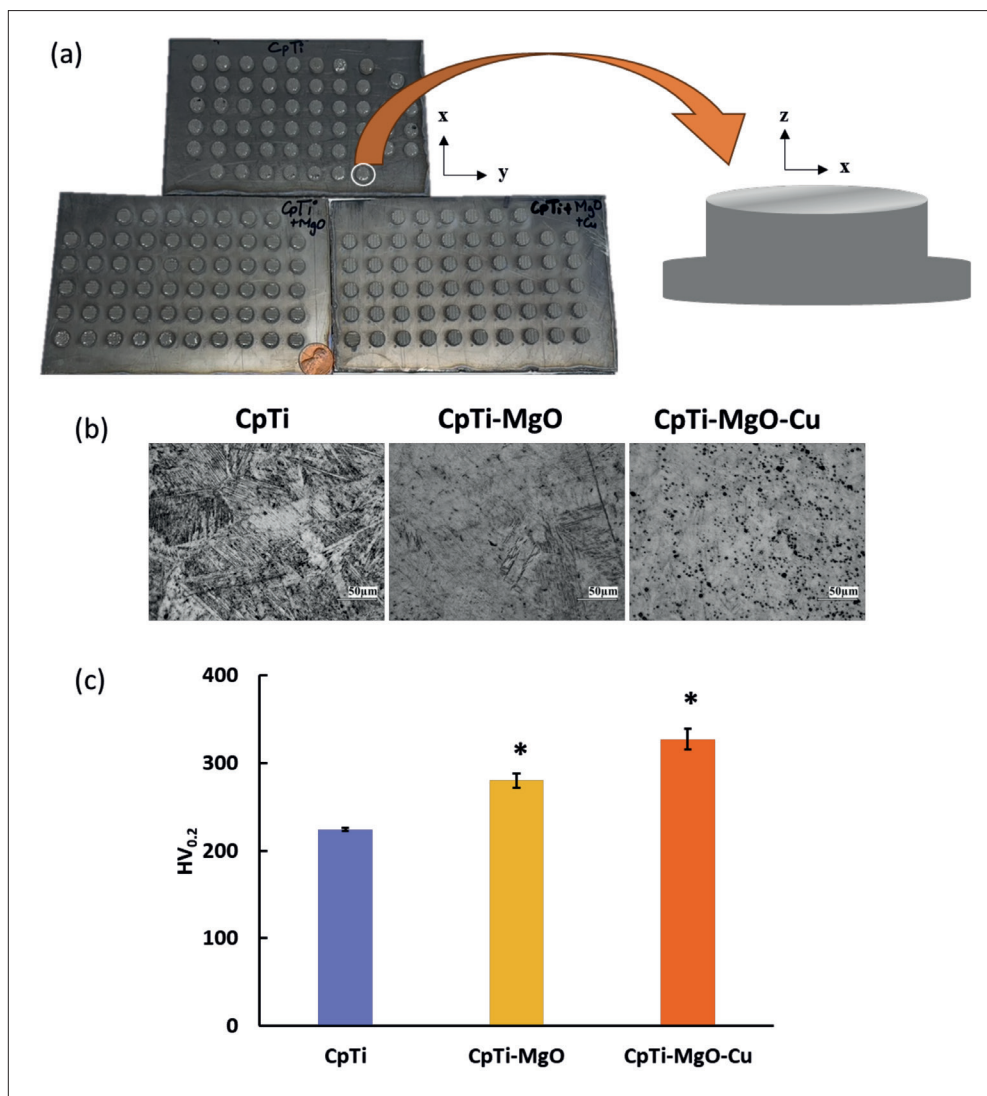
Figure 2. (a) An image of the build plate after DED operation showing dense discs printed on a CpTi build plate and a schematic of the top surface of the discs used for microstructure and microhardness evaluations. (b) Microstructure of polished samples, which are perpendicular to the build direction. The samples were processed via DED-based AM technique. CpTi and CpTi-MgO show α' martensitic acicular needle structure typically observed in AM-processed CpTi due to the fast cooling nature of the process. CpTi-MgO-Cu shows keyhole porosities on the surface due to balling effect and material splashing in the melt-pool owing to high thermal diffusivity and low laser absorption demonstrated by Cu. (c) Vickers microhardness ($HV_{0.2}$) evaluation of the compositions reveals enhancement in hardness with MgO addition in CpTi due to ceramic reinforcement. Hardness further increased with Cu addition in CpTi-MgO due to Ti_2Cu intermetallic formation. Hardness values were analyzed with one-way ANOVA test for n = 5 and α < 0.05. Tukey–Kramer correction simulation was carried out for pairwise comparison of means. $P < 0.05$ is considered significantly different and marked with an asterisk (*). Hardness values for all compositions were found to be statistically different from each other.

With Cu addition, we observed keyhole porosities owing to balling effect and splashing of molten material[43,44]. Cu has a high thermal diffusivity, almost 100 times that of Ti[43], and very poor laser absorption[38]. With the higher viscosity of Cu in the melt-pool compared to that of Ti[45-47], a shallower and wider melt-pool was created by splashing molten particles, leading to keyhole porosities.

Vickers microhardness measurements conducted on the polished surface of the DED-printed compositions (Figure 2c) revealed a hardness of 224 ± 2 $HV_{0.2}$ on CpTi surface, similar to those observed in a previous work[48]. With MgO addition in CpTi, the microhardness value increased to 280 ± 8 $HV_{0.2}$ due to reinforced MgO particles in the CpTi matrix providing resistance to deformation. Cu addition in CpTi-MgO increased the hardness to 327 ± 12 $HV_{0.2}$ due to Ti_2Cu intermetallic formation and solute solution strengthening by Cu solute atoms[49, 50].
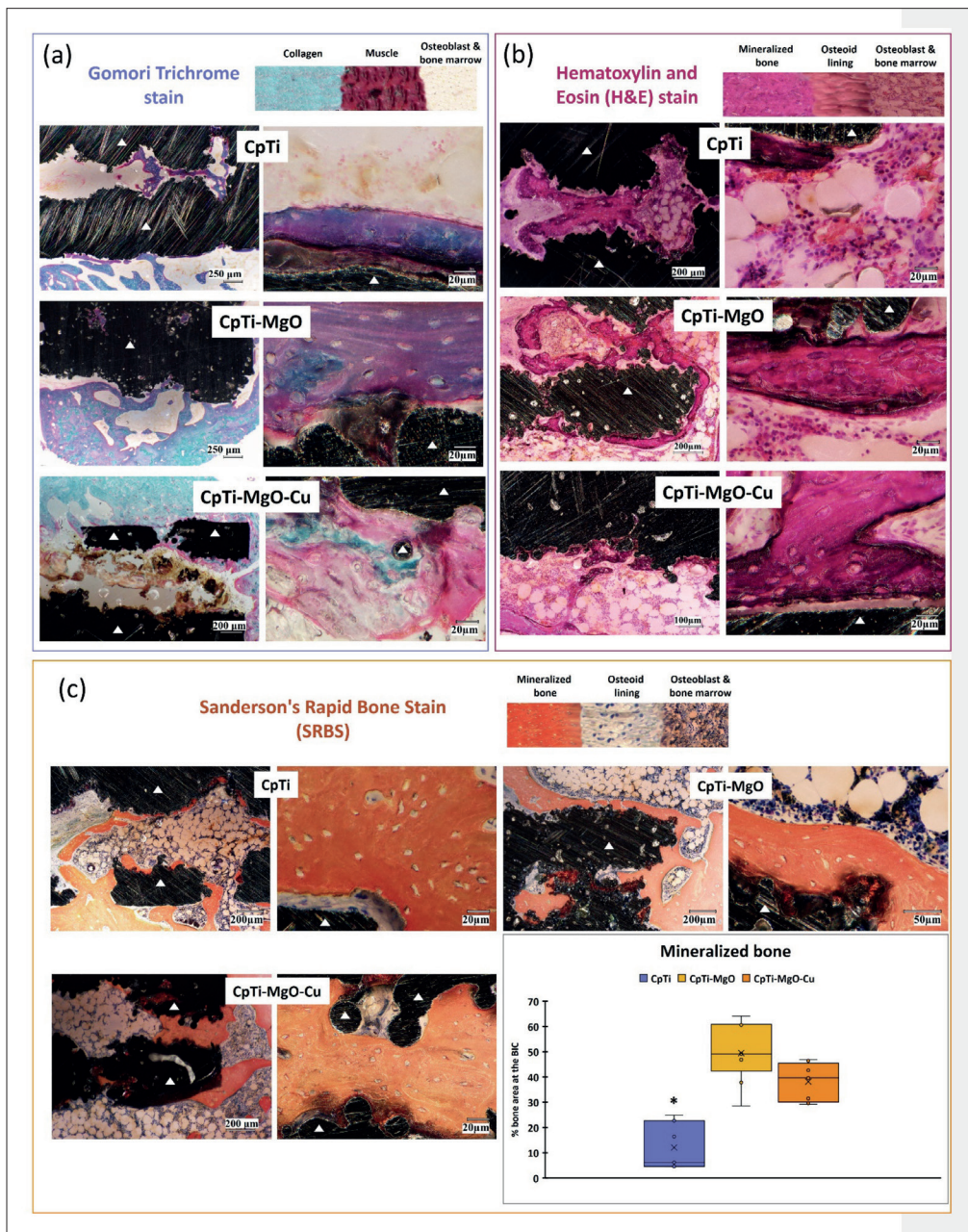
Figure 3. Histology images of *in vivo* bone sections of a rat distal femur model after 6 weeks of surgical implantation. A feature legend for each stain representing particular features is presented. The implant area is denoted by triangles in each histology image. (a) Gomori's trichrome stain represents the growth of muscle fibers and collagen formation at the bone-implant contact (BIC). Visible gaps were observed at the BIC for CpTi, indicating poor osseointegration performance. Similar gaps at the BIC for CpTi-MgO were filled with mineralization fronts. Muscle fiber interwoven with collagen formation apposed directly to the implant surface was observed for CpTi-MgO and CpTi-MgO-Cu. (b) Hematoxylin and Eosin (H&E) stain showing varying shades of pink, which indicate that bone remodeling is taking place. No inflammatory markers indicating necrosis or neoplasia were observed at the BIC. Trabecular bone formation apposed to the implant surface was observed in CpTi-MgO with good pore infiltration. CpTi-MgO-Cu showed a lower degree of trabecular bone at the BIC than CpTi-MgO, indicating delayed osseointegration owing to the presence of Cu. (c) Bone sections stained by Sanderson's rapid bone staining (SRBS) showed mineralized bone with well-embedded osteocytes apposed directly to the implant surface with infiltration into the implant region in CpTi-MgO. In contrast, CpTi showed an osteoid lining at the BIC, indicating delayed osseointegration compared to CpTi-MgO. Quantitative analysis of mineralized bone formation at the BIC showed four-fold bone formation for CpTi-MgO than CpTi. CpTi-MgO-Cu showed lower amounts of trabecular bone formation than CpTi-MgO, eliciting delayed osseointegration. Statistical analysis was performed with one-way ANOVA for mineralized bone formation for $n \geq 7$ and $\alpha < 0.05$. Tukey–Kramer simulations were conducted for pairwise comparison with a $P < 0.05$ considered to be significantly different. Mineralized bone formations for CpTi-MgO and CpTi-MgO-Cu were statistically similar and higher than that for CpTi. Low-power field images for all compositions and stains are presented in **Figure S1** (Supplementary File).

3.2. Histological analysis and histomorphometry: Bone-implant interface

To assess the biological performance of the compositions in a physiological environment, an *in vivo* rat model was utilized. CpTi was considered the control, while CpTi-MgO and CpTi-MgO-Cu were treated as the treatment compositions. Figure 3 presents bone sections of porous implants stained by Gomori's trichrome, H&E, and SRBS with approximately 40 vol.% porosity. H&E-stained bone sections (Figure 3b) were observed for possible inflammatory markers. None of the compositions show any inflammatory response, including neoplasia and necrosis[51]. Gomori's trichrome stain was employed to evaluate muscle fiber formation and collagen presence at the BIC (Figure 3a). At the BIC, all three compositions exhibited interwoven muscle fibers within collagenous regions, indicating early-stage osseointegration and mineralization front. Notably, these regions appeared visibly thinner for CpTi than CpTi-MgO and CpTi-MgO-Cu, suggesting a higher degree of osteogenesis in the latter compositions attributed to MgO. Further examination at higher magnification revealed gaps at the BIC for CpTi, whereas for CpTi-MgO and CpTi-MgO-Cu, these gaps were filled with osteogenic fronts accompanied by small areas of muscle fiber presence. Compared to CpTi-MgO and CpTi-MgO-Cu, the pink-bluish regions at the BIC for CpTi-MgO indicated the presence of muscle fibers interwoven with collagenous regions. Conversely, the bright pink regions at the BIC for CpTi-MgO-Cu indicated the presence of muscle fibers without collagen, suggesting delayed bone maturation and osseointegration due to the presence of Cu.

The observations described above are further supported by the H&E-stained histology micrographs (Figure 3b), where varying shades of pink and purple reveal distinct demarcations representing mineralized bone, osteoid lining, and osteoblast recruitment regions. In the case of CpTi, only certain regions exhibited a mineralized bone front at the BIC, while it was absent in other regions. In contrast, CpTi-MgO visibly demonstrated a higher presence of mineralized bone directly at the BIC, followed by an osteoid mineralization front, indicating superior early-stage osteogenic performance. Upon closer examination at the BIC, CpTi-MgO revealed the infiltration of mineralization fronts into the implant area, encompassing the implant regions. However, H&E histology for CpTi-MgO-Cu showed a lower degree of mineralized bone formation at the BIC compared to CpTi-MgO, although similar implant area infiltration features into the implant area were observed.

SRBS-stained histological micrographs, shown in Figure 3c, depict trabecular bone formation, osteoid presence, and osteoblast recruitment at the bone–implant interface. Across all compositions, mature bone formation with well-embedded osteocytes and focal outward growth of osteoblastic regions from the implant surface can be observed. CpTi's trabecular bone formation was followed by a thick osteoid lining at the BIC. In contrast, both CpTi-MgO and CpTi-MgO-Cu compositions exhibited newly formed trabecular bone directly apposed to the outer surface of the implant, indicating superior osseointegration performance compared to CpTi. Furthermore, the SRBS-stained histology micrographs reveal a higher degree of mature bone infiltration in the porous channel for CpTi-MgO and CpTi-MgO-Cu than CpTi. To obtain a clearer idea on the remodeling process undergone at the BIC, SRBS-stained histology was employed for histomorphometric analysis to evaluate the mature bone formation at the BIC (Figure 3c) within the specified ROI of 100 µm. Among the tested compositions, CpTi-MgO demonstrated the highest amount of matured bone formation at the BIC (49.5 ± 11.5%), followed by CpTi-MgO-Cu (38.2 ± 7.2%), while CpTi exhibited the least amount (12.1 ± 9.2%). This suggests a higher affinity and enhanced biological response of the host tissue toward the chemical makeup of CpTi-MgO and CpTi-MgO-Cu. Although the mature bone formation between CpTi-MgO and CpTi-MgO-Cu falls within the error range of each other, the difference in mean values can be attributed to the delayed osseointegration observed in the latter composition due to the presence of Cu, as discussed earlier.

3.3. Infection prevention

CpTi does not possess inherent antibacterial capability[52]. In order to address post-surgical infections, the addition of Cu was implemented in the CpTi-MgO composition. Cu is well-known for inhibiting bacterial growth through the on-contact killing of bacterial cells. Since *S. aureus* is one of the most commonly occurring infections *in vivo*[53], the antibacterial efficacy of the CpTi-MgO-Cu material against this bacterial strain at 24, 48, and 72 h time points using CpTi as the negative control was evaluated (Figure 4a). After 24 h of bacterial culture, we observed a significant reduction in bacterial viability on the agar plate for CpTi-MgO-Cu. Bacterial colony counting on the agar plate showed a 95% antibacterial efficiency for CpTi-MgO-Cu compared to CpTi. SEM images taken after 24, 48, and 72 h of culture revealed a significant reduction in planktonic bacteria on the surface of CpTi-MgO-Cu. At 24 h, the bacterial inhibition efficacy evaluated from the SEM images showed a 57% reduction in planktonic bacteria on the surface of CpTi-MgO-Cu. At 48 and 72 h, enhanced antibacterial efficacy was observed, with a 53 and 81% reduction in planktonic bacteria on the surface of CpTi-MgO-Cu, respectively. The SEM images at 48 and 72 h showed bacterial cells adhering to each other, which resulted in septum formation on the surface of CpTi-MgO-

Cu, indicating evidence of cytoplasmic outflow leading to eventual disruption of the bacterial cell membrane[54]. Higher magnification images (Figure 4b) revealed the on-contact bacterial killing of *S. aureus* on the surface of CpTi-MgO-Cu, with ruptured cell walls and disruption of the cell membrane, resulting in cytoplasm outflow and eventual killing of bacterial cells at 48 and 72 h time points.

CpTi-MgO-Cu demonstrated an excellent ability to inhibit infections at the end of the 72 h culture period.

4. Discussion

The volume of orthopedic surgeries has been experiencing an exponential rise, with over 7 million orthopedic surgeries performed in the United States alone[55,56]. According to a
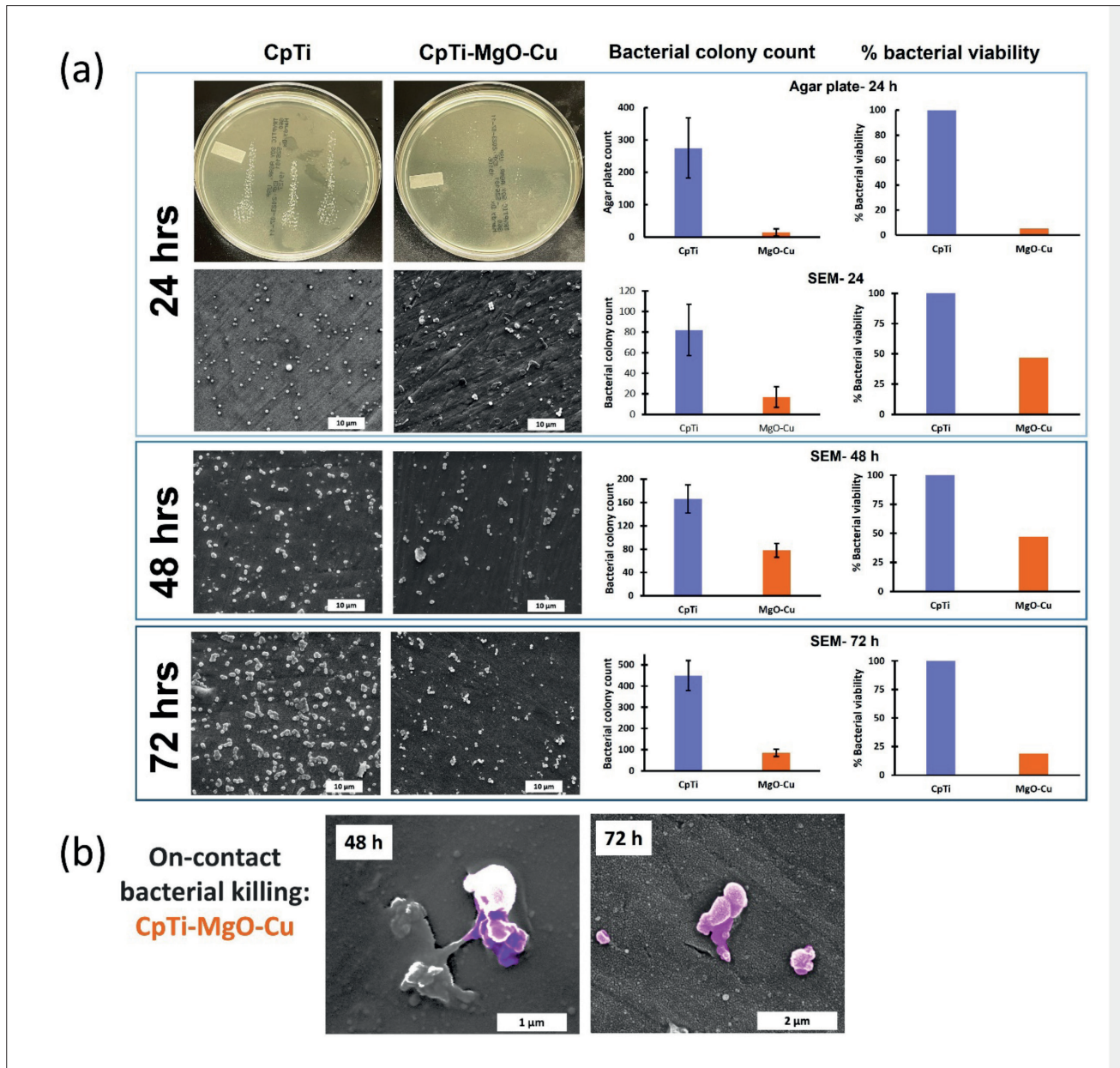

Figure 4. Results of antibacterial studies involving *Staphylococcus aureus* after 24, 48, and 72 h of culture. (a) Agar plate images after 24 h, and SEM images at 3000× magnification after 24, 48, and 72 h of culture. Respective bacterial colony counts and corresponding % bacterial viability relative to CpTi as the negative control are presented. Reduction in planktonic bacteria on the CpTi-MgO-Cu surface was significantly lower than on CpTi at all timepoints due to the bactericidal effect of Cu. Based on counting on SEM images (n = 4), there was a gradual reduction in % bacterial viability on CpTi-MgO-Cu from 24 to 72 h, with the highest antibacterial efficacy at 72 h. (b) High-magnification SEM images showing the on-contact bacterial killing of *S. aureus*, which manifested deflated cell morphology, ruptured cell membrane, and cytoplasm outflow 48 and 72 h after culture.

National Ambulatory Medical Care survey, 70% of patients visiting clinics for orthopedic surgery-related issues in 2015–2016 were over 45 years of age[57]. Age has a significant impact on the quality of recovery, as the quality of bone and its healing ability significantly decrease with age[58]. Elderly patients, who often suffer from immunocompromised bone health, usually have a prolonged recovery after surgery, which compromises their overall health. The infections at the implant site requiring revision surgery have a huge impact on the health of patients, particularly the individuals with age-related decline of bone health, leading to a further reduction in life expectancy. There is an unmet need in metallic implants for materials that can provide faster bone remodeling performance and infection prevention capabilities beyond what titanium currently offers. Current strategies include cemented implants with Ti6Al4V as the bulk material for strength with a surface coating of bioactive calcium phosphate or hydroxyapatite. Despite the superior *in vivo* performance toward early-stage osseointegration, one of the major shortcomings of cemented implants is delamination of the calcium phosphate coating due to poor metal-ceramic bonding. Instead, porous titanium metallic coating is a popular choice as it can abate the risk of coating failures[7]. In order to induce osteogenic properties in these porous titanium coatings, MgO addition in CpTi can potentially solve the coating failure issue.

4.1. Osteogenesis due to MgO addition
Mg plays an essential role in promoting bone calcification and remodeling. Mg deficiency in the bone has been linked with degenerative bone diseases such as osteoporosis[59,60]. Mg regulates intracellular calcium ion concentration, pH, transporters, enzymes, and protein synthesis[25,61]. Biodegradable Mg implants for low-load bearing bone–graft applications have been studied extensively[62,63]. Moreover, incorporating MgO in calcium phosphate has enhanced cellular proliferation *in vitro* and osteogenic performance *in vivo*[8,59]. In this study, incorporating MgO in CpTi enhanced osteogenesis at the bone–implant interface. With just 1 wt.% MgO addition in CpTi, mineralized bone formation at the BIC increased four-fold compared to that in CpTi (Figure 3c). Bone remodeling at the implant surface follows osteoblast recruitment followed by osteoid lining and eventual maturation of bone. CpTi histology images show an osteoid lining at the bone–implant interface. For CpTi-MgO, histology images show mineralized bone directly apposed to the implant's outer surface, indicating an enhanced bone remodeling process compared to CpTi. With superior osseointegration performance, we believe CpTi-MgO can potentially replace ceramic coatings in cemented implants and prevent coating failures.

4.2. Antibacterial performance due to Cu addition
Copper was used as a sterilizing agent for chest wounds, as recorded in Egyptian medical texts dating back 5000 years ago[64]. After it has been used for medical purposes in the generations that follow, the antibacterial potential of copper was discovered in the 19th century[65]. In 2011, copper was the first antimicrobial metallic material approved by the U.S. Environmental Protection Agency (EPA)[65]. Amid the COVID-19 pandemic, in 2021, U.S. EPA approved the use of copper-based disinfectants owing to the performance of copper and copper alloys against SARS-CoV-2, i.e., the virus responsible for COVID-19[66]. Realizing the potential of Cu as an antibacterial agent, extensive research has been conducted on incorporating Cu into Ti. Cu is a necessary trace element in the human body in a wide variety of tissues, but higher amounts of Cu can cause cytotoxicity leading to liver cirrhosis and neurologic abnormalities[67]. A debate persists on the optimum amount of Cu in Ti[68-71]. In this study, with 3 wt.% addition of Cu in CpTi, the H&E-stained bone sections show no signs of cytotoxicity. However, the mineralized bone formation in CpTi-MgO-Cu was observed to be lower than that in CpTi-MgO. Although 3 wt.% Cu did not cause cytotoxicity, there was a delayed early-stage osseointegration performance. CpTi-MgO-Cu still showed 3.5× mineralized bone formation at the interface than CpTi, showing superior osteogenic performance.

Early-stage osseointegration greatly affects the patient's recovery time. With CpTi-MgO-Cu used as a metallic coating on bulk Ti6Al4V alloy at load-bearing sites, coating failures in cemented implants can be avoided. At the same time, enhanced early-stage osseointegration can be achieved owing to the osteogenic properties of MgO, and inhibition of bacterial infections at the surgery site can prevent revision surgeries.

5. Conclusion
Early-stage osseointegration at the implant surface is critical in the post-surgery healing of elderly patients with degraded bone health. Bio-inertness and non-antibacterial nature of Ti result in aseptic loosening, which necessitates surgical intervention. Without adequate material intervention to enhance tissue integration and prevent polymicrobial infections, revision procedures would further degrade the patient's health and constitute a potential risk of morbidity. Ti6Al4V bulk implants coated with bioactive ceramics, such as osteogenic MgO and antibacterial Cu, tend to cause coating failures due to their weak metal-ceramic bonding. In this study, we propose the addition of 1 wt.% MgO and 3 wt.% Cu to

CpTi matrix, which is used as a coating on Ti6Al4V, to strengthen the Ti-on-Ti interface so as to prevent delamination failure. The *in vivo* studies demonstrated superior osteogenic performance of CpTi-MgO and CpTi-MgO-Cu compositions. Histomorphometric evaluations reveal 4× enhanced mineralized bone formation in CpTi-MgO (49.5 ± 11.5%) and 3.5× in CpTi-MgO-Cu (38.2 ± 7.2%) in comparison to CpTi (12.1 ± 9.2%) at the bone–implant interface. Additionally, 3 wt.% Cu addition did not result in cytotoxicity. Antibacterial studies using the commonly occurring *S. aureus* strain revealed that the Cu in CpTi-MgO-Cu composition had a bactericidal effect of 81% at the end of 72 h timepoint. Therefore, CpTi-MgO-Cu composition can be utilized as a multifaceted metal-ceramic coating on the bulk Ti6Al4V, which can serve as an ideal material for orthopedic implant applications to reduce implant failures and obviate the need for revision surgeries due to delayed early-stage osseointegration and infection-related issues.

Acknowledgments

Funding

Conflict of interest

The authors declare no conflict of interest.

Author contributions

Conceptualization: Amit Bandyopadhyay
Formal analysis: Sushant Ciliveri, Amit Bandyopadhyay
Investigation: Sushant Ciliveri
Methodology: Sushant Ciliveri, Amit Bandyopadhyay
Writing – original draft: Sushant Ciliveri
Writing – review & editing: Amit Bandyopadhyay

Ethics approval and consent to participate

All animal studies have been conducted after receiving necessary approval from the Institutional Animal Care and Use Committee (IACUC) of Washington State University (WSU) under the protocol number ASAF #6816.

Consent for publication

Not applicable.

Availability of data

All raw data for this study has been presented in this manuscript.

References

1. Liu X, Chu PK, Ding C, 2004, Surface modification of titanium, titanium alloys, and related materials for biomedical applications. *Mater Sci Eng R Rep,* 47(3): 49–121.

   https://doi.org/10.1016/j.mser.2004.11.001

2. Niinomi M, 2007, Recent research and development in metallic materials for biomedical, dental and healthcare products applications. *Mater Sci Forum*, 539: 193–200.

   https://doi.org/10.4028/0-87849-428-6.193

3. Van Noort R, 1987, Titanium: The implant material of today. *J Mater Sci,* 22(11): 3801–3811.

   https://doi.org/10.1007/BF01133326

4. Dong YP, Tang JC, Wang DW, *et al.*, 2020, Additive manufacturing of pure Ti with superior mechanical performance, low cost, and biocompatibility for potential replacement of Ti-6Al-4V. *Mater Des,* 196(2020): 109142.

   https://doi.org/10.1016/j.matdes.2020.109142

5. Feng J, Wei D, Zhang P, *et al.*, 2013, Preparation of TiNbTaZrMo high-entropy alloy with tunable Young's modulus by selective laser melting. *J Manuf Process,* 85(2023): 160–165.

   https://doi.org/10.1016/j.jmapro.2022.11.046

6. Cui Y-W, Chen L-Y, Chu Y-H, *et al.*, 2023, Metastable pitting corrosion behavior and characteristics of passive film of laser powder bed fusion produced Ti–6Al–4V in NaCl solutions with different concentrations. *Corros Sci,* 126(2022): 111017.

   https://doi.org/10.1016/j.corsci.2023.111017

7. Ciliveri S, Bandyopadhyay A, 2021, Influence of strut-size and cell-size variations on porous Ti6Al4V coated structures for load-bearing implants. *J Mech Behav Biomed Mater,* 105023.

   https://doi.org/10.1016/j.jmbbm.2021.105023

8. Ke D, Robertson SF, Dernell WS, *et al.*, 2017, Effects of MgO and SiO2 on plasma-sprayed hydroxyapatite coating: An in vivo study in rat distal femoral defects. *ACS Appl Mater Interfaces,* 9(31): 25731–25737.

   https://doi.org/10.1021/acsami.7b05574

9. Bandyopadhyay A, Bernard S, Xue W, *et al.*, 2006, Calcium phosphate-based resorbable ceramics: Influence of MgO, ZnO, and SiO2 dopants. *J Am Ceram Soc,* 89(9): 2675–2688.

   https://doi.org/10.1111/j.1551-2916.2006.01207.x

10. Fielding G, Bose S, 2013, SiO2 and ZnO dopants in three-dimensionally printed tricalcium phosphate bone tissue engineering scaffolds enhance osteogenesis and angiogenesis in vivo. *Acta Biomater,* 9(11): 9137–9148.

    https://doi.org/10.1016/j.actbio.2013.07.009

11. Libraty DH, Patkar C, Torres B, 2012, Staphylococcus aureus reactivation osteomyelitis after 75 years. *N Engl J Med,* 366(5): 481–482.

    https://doi.org/10.1056/NEJMc1111493

12. Macheras GA, Kateros K, Galanakos SP, *et al.*, 2011, The long-term results of a two-stage protocol for revision of an infected total knee replacement. *J Bone Joint Surg Br,* 93(11): 1487–1492.

    https://doi.org/10.1302/0301-620X.93B11.27319

13. Windsor RE, Insall JN, Urs WK, *et al.*, 1990, Two-stage reimplantation for the salvage of total knee arthroplasty complicated by infection. Further follow-up and refinement of indications. *J Bone Joint Surg Am,* 72(2): 272–278.

14. Buechel FF, 2004, The infected total knee arthroplasty: Just when you thought it was over. *J Arthroplasty,* 19(4 Suppl 1): 51–55.

    https://doi.org/10.1016/j.arth.2004.03.001

15. Zmistowski BM, 2013, *A Quarter of Patients Treated for PJI Dead Within 5 Years.*

    https://www.healio.com/news/orthopedics/20130104/a-quarter-of-patients-treated-for-pji-dead-within-5-years (accessed 2023-06-11).

16. O'Neill J, 2016, *Tackling Drug-Resistant Infections Globally: Final Report and Recommendations.* Government of the United Kingdom, United Kingdom.

    https://apo.org.au/node/63983 (accessed 2023-06-11).

17. Nishiguchi S, Nakamura T, Kobayashi M, *et al.*, 1999, The effect of heat treatment on bone-bonding ability of alkali-treated titanium. *Biomaterials,* 20(5): 491–500.

    https://doi.org/10.1016/S0142-9612(98)90203-4

18. Tang J, Wu Z, Yao X, *et al.,* 2022, From bio-inertness to osseointegration and antibacterial activity: A one-step micro-arc oxidation approach for multifunctional Ti implants fabricated by additive manufacturing. *Mater Des*, 221: 110962.

    https://doi.org/10.2139/ssrn.4121117

19. Costello RB, Rosanoff A, 2020, Magnesium, in *Present Knowledge in Nutrition (Eleventh Edition).* Marriott BP, Birt DF, Stallings VA, *et al.*, eds., Academic Press, Cambridge, MA, 349–373.

    https://doi.org/10.1016/B978-0-323-66162-1.00021-4

20. Staiger MP, Pietak AM, Huadmai J, *et al.*, 2006, Magnesium and its alloys as orthopedic biomaterials: A review. *Biomaterials,* 27(9): 1728–1734.

    https://doi.org/10.1016/j.biomaterials.2005.10.003

21. Xia X, Huang J, Wei J, *et al.*, 2022, Magnesium oxide regulates the degradation behaviors and improves the osteogenesis of poly(lactide-co-glycolide) composite scaffolds. *Compos Sci Technol,* 222: 109368.

    https://doi.org/10.1016/j.compscitech.2022.109368

22. Zhao Y, Liang H, Zhang S, *et al.*, 2020, Effects of magnesium oxide (MgO) shapes on in vitro and in vivo degradation behaviors of PLA/MgO composites in long term. *Polymers,* 12(5): 1074.

    https://doi.org/10.3390/polym12051074

23. Zreiqat H, Howlett CR, Zannettino A, *et al.*, 2002, Mechanisms of magnesium-stimulated adhesion of osteoblastic cells to commonly used orthopaedic implants. *J Biomed Mater Res,* 62(2): 175–184.

    https://doi.org/10.1002/jbm.10270

24. Niknam Z, Golchin A, Rezaei-Tavirani M, *et al.*, 2022, Osteogenic differentiation potential of adipose-derived mesenchymal stem cells cultured on magnesium oxide/polycaprolactone nanofibrous scaffolds for improving bone tissue reconstruction. *Adv Pharm Bull,* 12(1): 142–154.

    https://doi.org/10.34172/apb.2022.015

25. Roy M, Balla VK, Bandyopadhyay A, *et al.*, 2012, MgO-doped tantalum coating on Ti: Microstructural study and biocompatibility evaluation. *ACS Appl Mater Interfaces,* 4(2): 577–580.

    https://doi.org/10.1021/am201365e

26. Xue W, Dahlquist K, Banerjee A, *et al.*, 2008, Synthesis and characterization of tricalcium phosphate with Zn and Mg based dopants. *J Mater Sci Mater Med,* 19(7): 2669–2677.

    https://doi.org/10.1007/s10856-008-3395-4

27. Kim D-H, Shin K-K, Jung JS, *et al.*, 2015, The role of magnesium ion substituted biphasic calcium phosphate spherical micro-scaffolds in osteogenic differentiation of human adipose tissue-derived mesenchymal stem cells. *J Nanosci Nanotechnol,* 15(8): 5520–5523.

    https://doi.org/10.1166/jnn.2015.10463

28. 2017, Long-lived biomaterials. *Nat Biomed Eng,* 1(6): 1–1.

    https://www.nature.com/articles/s41551-017-0095#citeas

29. Mohammadi H, Sepantafar M, 2015, Ion-doped silicate bioceramic coating of Ti-based implant. *Iran Biomed J,* 20: 189–200.

    https://doi.org/10.7508/ibj.2016.04.002

30. Breme J, Zhou Y, Groh L, 1995, Development of a titanium alloy suitable for an optimized coating with hydroxyapatite. *Biomaterials,* 16(3): 239–244.

    https://doi.org/10.1016/0142-9612(95)92123-N

31. Guo L, Ataollah Naghavi S, Wang Z, *et al.*, 2022, On the design evolution of hip implants: A review. *Mater Des,* 216: 110552.

https://doi.org/10.1016/j.matdes.2022.110552

32. Lionberger D, Conlon C, Wattenbarger L, *et al.,* 2019, Unacceptable failure rate of a ceramic-coated posterior cruciate-substituting total knee arthroplasty. *Arthroplast Today,* 5(2): 187–192.

https://doi.org/10.1016/j.artd.2019.02.002

33. Bandyopadhyay A, Ciliveri S, Bose S, 2022, Metal additive manufacturing for load-bearing implants. *J Indian Inst Sci*, 102.1(2022): 561–584

https://doi.org/10.1007/s41745-021-00281-x

34. Traxel KD, Bandyopadhyay A, 2022, Selective laser melting of Ti6Al4V-B4C-BN in situ reactive composites. *J Mater Res Technol,* 18: 2654–2671.

https://doi.org/10.1016/j.jmrt.2022.03.092

35. Taniguchi N, Fujibayashi S, Takemoto M, *et al.*, 2016, Effect of pore size on bone ingrowth into porous titanium implants fabricated by additive manufacturing: An in vivo experiment. *Mater Sci Eng C,* 59: 690–701.

https://doi.org/10.1016/j.msec.2015.10.069

36. Ouyang P, Dong H, He X, *et al.*, 2019, Hydromechanical mechanism behind the effect of pore size of porous titanium scaffolds on osteoblast response and bone ingrowth. *Mater Des,* 183: 108151.

https://doi.org/10.1016/j.matdes.2019.108151

37. Imai K, Ikeshoji T-T, Sugitani Y, *et al.*, 2020, Densification of pure copper by selective laser melting process. *Mech Eng J,* 7(2): 19-00272-19–00272.

https://doi.org/10.1299/mej.19-00272

38. Guschlbauer R, Burkhardt AK, Fu Z, *et al.*, 2020, Effect of the oxygen content of pure copper powder on selective electron beam melting. *Mater Sci Eng A,* 779: 139106.

https://doi.org/10.1016/j.msea.2020.139106

39. Mitra I, Bose S, Dernell WS, *et al.*, 2021, 3D printing in alloy design to improve biocompatibility in metallic implants. *Mater Today,* 45: 20–34.

https://doi.org/10.1016/j.mattod.2020.11.021

40. Hall M, Frank E, Holmes G, *et al.*, 2009, The WEKA data mining software: An update. *ACM SIGKDD Explor Newsl,* 11(1): 10–18.

https://doi.org/10.1145/1656274.1656278

41. Arganda-Carreras I, Kaynig V, Rueden C, *et al.*, 2017, Trainable Weka segmentation: A machine learning tool for microscopy pixel classification. *Bioinformatics,* 33(15): 2424–2426.

https://doi.org/10.1093/bioinformatics/btx180

42. Afrouzian A, Groden CJ, Field DP, *et al.*, 2002, Additive manufacturing of Ti-Ni bimetallic structures. *Mater Des,* 215: 110461.

https://doi.org/10.1016/j.matdes.2022.110461

43. Newby E, Yadroitsava I, Krakhmalev P, *et al.*, 2019, Investigation of in-situ alloying grade 23 Ti with 5 at . % Cu by laser powder bed fusion for biomedical applications. *Mater Sci*, 197859609.

44. Svetlizky D, Das M, Zheng B, *et al.*, 2021, Directed energy deposition (DED) additive manufacturing: Physical characteristics, defects, challenges and applications. *Mater Today,* 49: 271–295.

https://doi.org/10.1016/j.mattod.2021.03.020

45. Assael MJ, Kalyva AE, Antoniadis KD, *et al.*, 2010, Reference data for the density and viscosity of liquid copper and liquid tin. *J Phys Chem Ref Data,* 39(3): 033105.

https://doi.org/10.1063/1.3467496

46. Paradis P-F, Ishikawa T, Yoda S, 2002, Non-contact measurements of surface tension and viscosity of niobium, zirconium, and titanium using an electrostatic levitation furnace. *Int J Thermophys,* 23(3): 825–842.

https://doi.org/10.1023/A:1015459222027

47. Mosallanejad MH, Niroumand B, Aversa A, *et al.*, 2021, Laser powder bed fusion in-situ alloying of Ti-5%Cu alloy: Process-structure relationships. *J Alloys Compd,* 857: 157558.

https://doi.org/10.1016/j.jallcom.2020.157558

48. Ciliveri S, Mitra I, Bose S, *et al.*, 2022, Effects of oxide ceramic addition on biocompatibility of titanium, in *Metal-Matrix Composites*, Srivatsan TS, Rohatgi PK, Hunyadi Murph S, eds., Springer International Publishing, Cham, 323–334.

https://doi.org/10.1007/978-3-030-92567-3_20

49. Onuike B, Heer B, Bandyopadhyay A, 2018, Additive Manufacturing of Inconel 718 – Copper Alloy Bimetallic Structure using Laser Engineered Net Shaping. *Addit Manuf*, 21: 133–140.

https://doi.org/10.1016/j.addma.2018.02.007

50. Kikuchi M, Takada Y, Kiyosue S, *et al.*, 2003, Mechanical properties and microstructures of cast Ti–Cu alloys. *Dent Mater,* 19(3): 174–181.

https://doi.org/10.1016/S0109-5641(02)00027-1

51. Zhang L, Chang M, Beck CA, *et al.*, 2016, Analysis of new bone, cartilage, and fibrosis tissue in healing murine allografts using whole slide imaging and a new automated histomorphometric algorithm. *Bone Res,* 4: 15037.

https://doi.org/10.1038/boneres.2015.37

52. Itabashi T, Narita K, Ono A, *et al.*, 2017, Bactericidal and antimicrobial effects of pure titanium and titanium alloy treated with short-term, low-energy UV irradiation. *Bone Jt Res,* 6(2): 108–112.

https://doi.org/10.1302/2046-3758.62.2000619

53. Arciola CR, Campoccia D, Montanaro L, 2018, Implant infections: Adhesion, biofilm formation and immune evasion. *Nat Rev Microbiol*, 16(7): 397–409.

    https://doi.org/10.1038/s41579-018-0019-y

54. O'Driscoll NH, Cushnie TPT, Matthews KH, *et al.*, 2018, Colistin causes profound morphological alteration but minimal cytoplasmic membrane perforation in populations of Escherichia coli and Pseudomonas aeruginosa. *Arch Microbiol*, 200(5): 793–802.

    https://doi.org/10.1007/s00203-018-1485-3

55. Centeno C, 2021, *The Evidence Supporting Common Orthopedic Surgeries Is AWFUL*. Regenexx.

    https://regenexx.com/blog/the-evidence-supporting-common-orthopedic-surgeries-is-awful/ (accessed 2023-06-20).

56. Shukla D, Patel S, Clack L, *et al.*, 2021, Retrospective analysis of trends in surgery volumes between 2016 and 2019 and impact of the insurance deductible: Cross-sectional study. *Ann Med Surg*, 63: 102176.

    https://doi.org/10.1016/j.amsu.2021.02.022

57. Orthopedic Surgery Fact Sheet from the National Ambulatory Medical Care Survey.

    https://www.cdc.gov/nchs/data/namcs/factsheets/NAMCS-2015-16-Orthopedic-Surgery-508.pdf

58. Clark D, Nakamura M, Miclau T, *et al.*, 2017, Effects of aging on fracture healing. *Curr Osteoporos Rep*, 15(6): 601–608.

    https://doi.org/10.1007/s11914-017-0413-9

59. Tarafder S, Dernell WS, Bandyopadhyay A, *et al.*, 2015, SrO- and MgO-doped microwave sintered 3D printed tricalcium phosphate scaffolds: Mechanical properties and in vivo osteogenesis in a rabbit model. *J Biomed Mater Res B Appl Biomater*, 103(3): 679–690.

    https://doi.org/10.1002/jbm.b.33239

60. Nandi SK, Roy M, Bandyopadhyay A, *et al.*, 2023, In vivo biocompatibility of SrO and MgO doped brushite cements. *J Biomed Mater Res B Appl Biomater*, 111(3): 599–609.

    https://doi.org/10.1002/jbm.b.35177

61. Schmitz C, Deason F, Perraud A-L, 2007, Molecular components of vertebrate Mg2+-homeostasis regulation. *Magnes Res*, 20(1): 6–18.

62. Singh S, Vashisth P, Shrivastav A, *et al.*, 2019, Synthesis and characterization of a novel open cellular Mg-based scaffold for tissue engineering application. *J Mech Behav Biomed Mater*, 94(2019): 54–62.

    https://doi.org/10.1016/j.jmbbm.2019.02.010

63. Chakraborty Banerjee P, Al-Saadi S, Choudhary L, *et al.*, 2019, Magnesium implants: Prospects and challenges. *Materials*, 12(1): 136.

    https://doi.org/10.3390/ma12010136

64. Dollwet HHA, Sorenson JRJ, 1985, Historic uses of copper compounds in medicine. *Trace Elem Med*, 2(2): 80–87.

65. Grass G, Rensing C, Solioz M, 2011, Metallic copper as an antimicrobial surface. *Appl Environ Microbiol*, 77(5): 1541–1547.

    https://doi.org/10.1128/AEM.02766-10

66. EPA Press Office, 2021, *EPA Registers Copper Surfaces for Residual Use Against Coronavirus*.

    https://www.epa.gov/newsreleases/epa-registers-copper-surfaces-residual-use-against-coronavirus (accessed 2023-06-20).

67. Tchounwou PB, Newsome C, Williams J, *et al.*, 2008, Copper-induced cytotoxicity and transcriptional activation of stress genes in human liver carcinoma (HepG2) cells. *Met Ions Biol Med*, 10: 285–290.

68. Liu R, Memarzadeh K, Chang B, *et al.*, 2016, Antibacterial effect of copper-bearing titanium alloy (Ti-Cu) against *Streptococcus Mutans* and *Porphyromonas gingivalis*. *Sci Rep*, 6: 29985.

    https://doi.org/10.1038/srep29985

69. Liu R, Tang Y, Zeng L, *et al.*, 2018, In vitro and in vivo studies of antibacterial copper-bearing titanium alloy for dental application. *Dent Mater*, 34(8): 1112–1126.

    https://doi.org/10.1016/j.dental.2018.04.007

70. Zhang E, Li F, Wang H, *et al.*, 2013, A new antibacterial titanium–copper sintered alloy: Preparation and antibacterial property. *Mater Sci Eng C*, 33(7): 4280–4287.

    https://doi.org/10.1016/j.msec.2013.06.016

71. Liu J, Li F, Liu C, *et al.*, 2014, Effect of Cu content on the antibacterial activity of titanium–copper sintered alloys. *Mater Sci Eng C*, 35(2014): 392–400.

    https://doi.org/10.1016/j.msec.2013.11.028